



Published in final edited form as:

Comput Med Imaging Graph. 2008 July ; 32(5): 353–366.

Generalized Fuzzy Clustering for Segmentation of Multi-Spectral Magnetic Resonance Images

Renjie He, Ph.D.,

Department of Diagnostic and Interventional Imaging, University of Texas Medical School at Houston, 6431 Fannin Street, Houston, TX 77030, Tel: (713)500-7621, Fax: (713)500-7684, Email: Renjie.He@uth.tmc.edu

Sushmita Datta, Ph.D.,

Department of Diagnostic and Interventional Imaging, University of Texas Medical School at Houston, 6431 Fannin Street, Houston, TX 77030, Tel: (713)500-7597, Fax: (713)500-7684, Email: Sushmita.Datta@uth.tmc.edu

Balasarivasa Rao Sajja, Ph.D., and

Department of Diagnostic and Interventional Imaging, University of Texas Medical School at Houston, 6431 Fannin Street, Houston, TX 77030, Tel: (713)500-7680, Fax: (713)500-7684, Email: Balasarivasa.R.Sajja@uth.tmc.edu

Ponnada A. Narayana, Ph.D.

Department of Diagnostic and Interventional Imaging, University of Texas Medical School at Houston, 6431 Fannin Street, Houston, TX 77030, Tel: (713)500-7677, Fax: (713)500-7684, Email: Ponnada.A.Narayana@uth.tmc.edu

Abstract

An integrated approach for multi-spectral segmentation of MR images is presented. This method is based on the fuzzy c-means (FCM) and includes bias field correction and contextual constraints over spatial intensity distribution and accounts for the non-spherical cluster's shape in the feature space. The bias field is modeled as a linear combination of smooth polynomial basis functions for fast computation in the clustering iterations. Regularization terms for the neighborhood continuity of intensity are added into the FCM cost functions. To reduce the computational complexity, the contextual regularizations are separated from the clustering iterations. Since the feature space is not isotropic, distance measure adopted in Gustafson-Kessel (G-K) algorithm is used instead of the Euclidean distance, to account for the nonspherical shape of the clusters in the feature space. These algorithms are quantitatively evaluated on MR brain images using the similarity measures.

Keywords

Adaptive FCM; Contextual constraints; G-K algorithm; Inhomogeneity field; Multispectral segmentation; MRI; Similarity measures

Correspondence to: Renjie He.

Publisher's Disclaimer: This is a PDF file of an unedited manuscript that has been accepted for publication. As a service to our customers we are providing this early version of the manuscript. The manuscript will undergo copyediting, typesetting, and review of the resulting proof before it is published in its final citable form. Please note that during the production process errors may be discovered which could affect the content, and all legal disclaimers that apply to the journal pertain.

1. Introduction

The superb soft tissue contrast seen on magnetic resonance imaging (MRI) is ideally suited for tissue classification and volumetry. This has significant implications in understanding the neural basis for many neurological disorders [19]. For instance, in a number of neurological disorders, such as multiple sclerosis (MS) and Alzheimer's disease, the volume changes in total brain, gray matter (GM), and white matter (WM) provide important information about the neuronal and axonal loss [4,25,26]. In addition, MRI-derived tissue volumetry is increasingly employed as a secondary end point in many clinical trials [22]. Accurate and robust tissue classification or segmentation is critical for detecting changes in tissue volumes in healthy and diseased brain. Commonly used techniques for segmentation have been recently reviewed [24].

A unique feature of MRI is its multi-model nature that allows acquisition of images with different tissue contrasts (T1-, T2-, density-weighting etc.) It is possible to improve the quality of segmentation by combining information from images with multiple contrasts [3,13,16,32]. Feature map-based classification techniques for MR image segmentation have attracted considerable attention because they are fast, simple to implement, and allow expert's input in tissue classification. However, in practice, this multi-spectral segmentation is prone to false tissue classifications and requires significant manual intervention and pre-processing since the distribution of intensities in the feature space is distorted by various factors that include image intensity inhomogeneity arising from the radio frequency receiver and transmitter coil profiles, partial volume averaging effects from the limited resolution, image noise, and spatial misalignment of images. While there are a few methods to overcome some of these problems, we focus on fuzzy c-means (FCM) based methods [1,8,10,23,27,28,31,33] because of their many desirable features in tissue classification.

Conventional FCM-based methods do not correct the intensity inhomogeneity and do not exploit contextual information. The adaptive FCM (AFCM) incorporates the intensity inhomogeneity correction, contextual constraints to overcome the noise problems and fuzzy membership to address the partial volume averaging effect, and automatic clustering [1,20,23,27,28,30,34].

One essential problem with adaptive FCM (and a number of other clustering algorithms) is that they are totally based on the objective cost function. Therefore, the performance of the algorithms is greatly dependent on the way the objective cost function is constructed. When using the Euclidean distance in the objective cost function, as in FCM, the algorithm has a tendency to generate equal cluster volumes with spherical occupancy in the feature space [8,14]. This could have a significant effect on the MRI segmentation results. To deal with this problem, a few methods have been proposed in MR image segmentation in which some pre-selected seeds are included [5,6]. Methods aimed at automating the selection of seeds are proposed by Sucking et al. [30]. However, these methods are cumbersome to implement. In order to automatically produce reasonable clusters, more sophisticated distance measure is included in the Gustafson-Kessel (G-K) algorithm [15,17] in which a positive definite, symmetric scatter matrix (or covariance matrix) is used instead of the Euclidean distance to define the Mahalanobis distance to form an ellipsoidal cluster in the feature space. In the G-K algorithm each cluster is characterized by a symmetric and positive definite matrix for automatic adaptation of each individual cluster volume.

The fundamentals of fuzzy clustering in medical image segmentation are well described in Sutton et al. [31]. The main formalism presented in this paper is based on the grouped coordinate descent method (also called alternating optimization (AO)) [31]. Important details, such as singularity, initialization, rules of thumb for the parameters, methods to determine the

number of clusters are not described in this paper due to space limitation, but can be found elsewhere [17]. Throughout this paper, we assumed that the total number of clusters is known and that proper initialization is available.

In the current studies, we extended AFCM to multispectral segmentation that included efficient intensity non-uniformity (or bias field) correction and contextual constraints over neighborhood spatial intensity distribution. The nonspherical occupancy of the feature space was accounted by utilizing cluster scatter measures to define the Mahalanobis distance. This method was applied to segment GM, WM and CSF of MR images acquired with fast spin echo (FSE) pulse sequence which is commonly used in the routine clinical practice. The performance of the algorithm was quantitatively evaluated using similarity measures.

2. Methods and Materials

2.1. Multi-spectral adaptive FCM

This section describes the extension of the original adaptive FCM [1] to multi-spectral case with the inclusion of contextual constraints [1][27] to obtain a general cost function. This extension to the original AFCM is referred to as generalized FCM (GFCM). The objective function of the conventional FCM for clustering n -channel image data, \mathbf{x}_k , $k = 1, \dots, N$, into c -classes can be expressed as

$$J = \sum_{i=1}^c \sum_{k=1}^N u_{ik}^p \|\mathbf{x}_k - \mathbf{v}_i\|^2 \quad (1)$$

subject to

$$\sum_{i=1}^c u_{ik} = 1, u_{ik} \in [0, 1], 0 < \sum_{k=1}^N u_{ik} < N. \quad (2)$$

where u_{ik} is the membership of k -th voxel belonging to class- i , \mathbf{v}_i is the cluster center of class- i , and p is a preset weighting exponent or fuzzifier. To include the influence of immediate neighborhood for forcing the solution towards piecewise-homogeneous labeling, regularization terms are introduced into the objective function as suggested by others [1, 20, 27]. With the inclusion of the regularization terms, Eq. (1) can be written as

$$J_m = \sum_{i=1}^c \sum_{k=1}^N u_{ik}^p \|\mathbf{x}_k - \mathbf{v}_i\|^2 + \sum_{i=1}^c \sum_{k=1}^N u_{ik}^p \left(\sum_{\mathbf{x}_r \in N_k} \left(\frac{\alpha}{N_R} \|\mathbf{x}_r - \mathbf{v}_i\|^2 \right) \right) \quad (3)$$

where N_k represents the neighbors of current voxel, and N_R is the cardinality of N_k . The regularization term can be adjusted by setting the value of α corresponding to neighborhood constraints in Eq. (3) to compromise between the sharp segmentation and the pulse noise [1, 27].

In general, the distribution of MR image intensities in the feature space is distorted due to the presence of bias field that needs to be corrected for proper tissue classification. The intensity of a voxel located at the spatial position k ($k = 1, \dots, N$, where N is the number of voxels) can be represented as [28]

$$\mathbf{o}_k = \mathbf{G}_k \mathbf{t}_k + \text{noise}(k) \quad (4)$$

where \mathbf{o}_k is the observed intensity, \mathbf{t}_k is the true intensity, \mathbf{G}_k is the diagonal matrix representing the gain field, and $\text{noise}(k)$ is the noise. Since we are mainly interested in multi-spectral case, all the above variables, except \mathbf{G}_k , are vectors. Assuming n image channels, we can explicitly express $\mathbf{o}_k = [o_{k1}, o_{k2}, \dots, o_{kn}]^T$ and $\mathbf{t}_k = [t_{k1}, t_{k2}, \dots, t_{kn}]^T$. The gain field can be denoted as $\mathbf{g}_k = [g_{k1}, g_{k2}, \dots, g_{kn}]^T$, with $\mathbf{G}_k = \text{diag}(g_{k1}, g_{k2}, \dots, g_{kn})$ and Eq. (4) can be rewritten as

$$[o_{k1}, \dots, o_{kn}]^T = [g_{k1}t_{k1}, \dots, g_{kn}t_{kn}]^T + \text{noise}(k). \quad (5)$$

By ignoring the noise term and applying the log-transform on both sides of Eq. (5), denoting the log-transformed observed MR image data as \mathbf{y}_k and the log-transformed true intensity of underlying tissues as \mathbf{x}_k , the MR image data can be approximated as [1,23]

$$\mathbf{y}_k = \mathbf{b}_k + \mathbf{x}_k \quad (6)$$

where $\mathbf{b}_k = [b_{k1}, b_{k2}, \dots, b_{kn}]^T$ is the vectorial voxel representation of the bias field.

Generally, the bias field can be approximated as $b_{kl} = \sum_i q_{li} \phi_i(p_k)$ where $\phi_i(p_k)$ is a smooth basis function and p_k represents the coordinates. Therefore \mathbf{b}_k can be written as

$$\mathbf{b}_k = \left[\sum_i q_{1i} \phi_i(p_k), \sum_i q_{2i} \phi_i(p_k), \dots, \sum_i q_{ni} \phi_i(p_k) \right]^T = \mathbf{Q}\Phi(p_k) \quad (7)$$

with

$$\Phi(p_k) = [\varphi_1(p_k), \varphi_2(p_k), \dots, \varphi_m(p_k)]^T,$$

and

$$\mathbf{Q} = \begin{bmatrix} q_{11} & q_{12} & \cdots & q_{1m} \\ q_{21} & q_{22} & \cdots & q_{2m} \\ \vdots & \vdots & \cdots & \vdots \\ q_{n1} & q_{n2} & \cdots & q_{nm} \end{bmatrix}$$

where m is the number of basis functions in Φ . The whole bias field can be expressed as

$$\mathbf{B} = [\mathbf{b}_1, \mathbf{b}_2, \dots, \mathbf{b}_{N-1}, \mathbf{b}_N]. \quad (8)$$

In practice, the approximation of the bias field is over the 3D space and the spatial relation have to be included into the expansion of the smooth basis functions.

By the piecewise homogeneous assumption, the influence of the bias field is included in the objective function (Eq. 3). Introducing a normalizing factor \mathbf{e} , the modified objective function can be written as

$$J_m = \sum_{i=1}^c \sum_{k=1}^N u_{ik}^p \|\mathbf{y}_k - \mathbf{Q}\Phi(p_k) + \mathbf{e} - \mathbf{v}_i\|^2 + \sum_{i=1}^c \sum_{k=1}^N u_{ik}^p \left(\sum_{\mathbf{x}_r \in \mathcal{N}_k} \left(\frac{\alpha}{N_R} \|\mathbf{y}_r - \mathbf{Q}\Phi(p_r) + \mathbf{e} - \mathbf{v}_i\|^2 \right) \right) \quad (9)$$

subject to

$$\sum_{i=1}^c u_{ik} = 1, u_{ik} \in [0, 1], 0 < \sum_{k=1}^N u_{ik} < N.$$

Since the amplitude, \mathbf{b}_k , is arbitrary, normalization of \mathbf{b}_k is necessary to ascertain that the sum of \mathbf{b}_k is zero to satisfy the convergence condition of *alternating optimization* (AO). The normalization factor, \mathbf{e} , will maintain the sum of \mathbf{b}_k to zero and plays an important role in the convergence of the iterations in the AO that can be applied to Eq. (9) to arrive at the (local) optima. The image segmentation is achieved by solving

$$\min_{\{u_{ik}\}, \{\mathbf{v}_i\}_{i=1}^c, \{\mathbf{b}_k\}_{k=1}^N} J_m, \quad \text{subject to} \quad \sum_{i=1}^c u_{ik} = 1. \quad (10)$$

2.2. Extension of AFCM algorithm with G-K measure

Since the Euclidean distance measure is used in the objective function to compute the distance between data points and prototypes of clusters, FCM method works well for the spherical shaped clusters with equal volumes. To take the cluster shape into consideration, we incorporate the covariance matrix of each cluster into the calculation of distance measures using Gustafson-Kessel (G-K) algorithm as described in the following section.

In the G-K algorithm, a more sophisticated distance measure, the Mahalanobis distance, based on positive definite, symmetric scatter matrix (or covariance matrix) is used to account for the scatter shape of each cluster and the ellipsoidal occupancy of clusters in the feature space [15]. The fuzzy covariance matrix, \mathbf{S}_i , is given by [15,17]

$$\mathbf{S}_i = \frac{\sum_{k=1}^N u_{ik}^p (\mathbf{y}_k - \mathbf{Q}\Phi(p_k) + \mathbf{e} - \mathbf{v}_i) (\mathbf{y}_k - \mathbf{Q}\Phi(p_k) + \mathbf{e} - \mathbf{v}_i)^T}{\sum_{k=1}^N u_{ik}^p} \quad (11)$$

We describe the algorithm for extending the G-K algorithm to multi-channel MR image segmentation by denoting

$$D_{ik} = (\mathbf{y}_k - \mathbf{Q}\Phi(p_k) + \mathbf{e} - \mathbf{v}_i)^T \mathbf{A}_i (\mathbf{y}_k - \mathbf{Q}\Phi(p_k) + \mathbf{e} - \mathbf{v}_i) \quad (12)$$

and

$$\Upsilon_{ik} = \sum_{\mathbf{y}_r \in N_k} \left(\frac{\alpha}{N_R} (\mathbf{y}_r - \mathbf{Q}\Phi(p_r) + \mathbf{e} - \mathbf{v}_i)^T \mathbf{A}_i (\mathbf{y}_r - \mathbf{Q}\Phi(p_r) + \mathbf{e} - \mathbf{v}_i) \right). \quad (13)$$

where $\mathbf{A}_i = \sqrt[n]{\det(\mathbf{S}_i)} \mathbf{S}_i^{-1}$ [15,17] denotes the norm matrix. The Lagrangean multiplier is adopted to include the constraints into the optimization, and the augmented objective function becomes

$$F_m = \sum_{i=1}^c \sum_{k=1}^N (u_{ik}^p D_{ik} + u_{ik}^p \Upsilon_{ik}) + \lambda \left(1 - \sum_{i=1}^c u_{ik} \right). \quad (14)$$

Taking the derivative of F_m with respect to u_{ik} for $p > 1$, and equating to zero, and with the

$$\text{constraint } \sum_{j=1}^c u_{jk} = 1, \quad \text{we get}$$

$$u_{ik} = 1 \left/ \sum_{j=1}^c \left(\frac{D_{ik} + \Upsilon_{ik}}{D_{jk} + \Upsilon_{jk}} \right)^{1/(p-1)} \right. . \quad (15)$$

For a positive definite matrix \mathbf{L} , for any vector \mathbf{x} , we know that

$$\frac{\partial}{\partial \mathbf{x}} (\mathbf{x}^T \mathbf{L} \mathbf{x}) = 2\mathbf{L}\mathbf{x}. \quad (16)$$

Taking the derivative of F_m with respect to \mathbf{v}_i and equating to zero, and using the result in Eqn. (16) with the property $\mathbf{A}_i^{-1} \mathbf{A}_i = \mathbf{I}$, we have

$$\mathbf{v}_i = \frac{\sum_{k=1}^N u_{ik}^p \left((\mathbf{y}_k - \mathbf{Q}\Phi(p_k) + \mathbf{e}) + \frac{\alpha}{N_R} \sum_{\mathbf{y}_r \in N_k} (\mathbf{y}_r - \mathbf{Q}\Phi(p_r) + \mathbf{e}) \right)}{(1+\alpha) \sum_{k=1}^N u_{ik}^p} \quad (17)$$

Similarly, the bias field can be estimated by equating the derivative of F_m with respect to \mathbf{b}_k to zero and using the matrix derivative result

$$\frac{\partial}{\partial \mathbf{X}} (\mathbf{X}\mathbf{a} + \mathbf{b})^T \mathbf{L} (\mathbf{X}\mathbf{a} + \mathbf{b}) = (\mathbf{L} + \mathbf{L}^T) (\mathbf{X}\mathbf{a} + \mathbf{b}) \mathbf{a}^T, \quad (18)$$

we have

$$\begin{aligned} & \sum_{i=1}^c \sum_{k=1}^N u_{ik}^p (\mathbf{A}_i + \mathbf{A}_i^T) \mathbf{Q} ([\Phi(p_k)] [\Phi(p_k)]^T + \sum_{y_r \in N_k} \frac{\alpha}{N_R} [\Phi(p_r)] [\Phi(p_r)]^T) \\ &= \sum_{i=1}^c \sum_{k=1}^N u_{ik}^p (\mathbf{A}_i + \mathbf{A}_i^T) ((\mathbf{y}_k + \mathbf{e} - \mathbf{v}_i) [\Phi(p_k)]^T + \sum_{y_r \in N_k} \frac{\alpha}{N_R} (\mathbf{y}_r + \mathbf{e} - \mathbf{v}_i) [\Phi(p_r)]^T) \end{aligned} \quad (19)$$

Let

$$\mathbf{O}_i = (\mathbf{A}_i + \mathbf{A}_i^T), \quad (20)$$

$$\mathbf{M}_i = \sum_{k=1}^N u_{ik}^p ([\Phi(p_k)] [\Phi(p_k)]^T + \sum_{y_r \in N_k} \frac{\alpha}{N_R} [\Phi(p_r)] [\Phi(p_r)]^T), \quad (21)$$

$$\text{and } \mathbf{R} = \sum_{i=1}^c \sum_{k=1}^N u_{ik}^p (\mathbf{A}_i + \mathbf{A}_i^T) ((\mathbf{y}_k + \mathbf{e} - \mathbf{v}_i) [\Phi(p_k)]^T + \sum_{y_r \in N_k} \frac{\alpha}{N_R} (\mathbf{y}_r + \mathbf{e} - \mathbf{v}_i) [\Phi(p_r)]^T). \quad (22)$$

Eq. (19) can be written as

$$\mathbf{O}_1 \mathbf{Q} \mathbf{M}_1 + \mathbf{O}_2 \mathbf{Q} \mathbf{M}_2 + \dots + \mathbf{O}_c \mathbf{Q} \mathbf{M}_c = \mathbf{R} \quad (23)$$

which equals to

$$(\mathbf{O}_1 \otimes \mathbf{M}_1^T + \mathbf{O}_2 \otimes \mathbf{M}_2^T + \dots + \mathbf{O}_c \otimes \mathbf{M}_c^T) \mathbf{Q} := \mathbf{R}, \quad (24)$$

where \otimes represents the Kronecker product in Eqn. (24). The definition of “:” in Eqn. (24) is as follow: for arbitrary matrix \mathbf{W} , the note “ $\mathbf{W}:$ ” is defined as the vector formed by concatenating all the columns of matrix \mathbf{W} , e.g. if $\mathbf{h} = \mathbf{W}_{[m \times n]}$, then $h_{i+m(j-1)} = w_{i,j}$. Therefore we have

$$\mathbf{Q} := \left(\sum_{i=1}^c \mathbf{O}_i \otimes \mathbf{M}_i^T \right)^{-1} \mathbf{R}, \quad (25)$$

The computation of \mathbf{Q} is fast since the dimensions of \mathbf{O} and \mathbf{M} are small. The above solutions lead to the smooth approximation of the bias field as

$$\begin{aligned} \mathbf{b}_{k(\text{smooth})} &= \left[\sum_i q_{1i} \varphi_i(p_k), \sum_i q_{2i} \varphi_i(p_k), \dots, \sum_i q_{ni} \varphi_i(p_k) \right]^T \\ &= \mathbf{Q} \Phi(p_k) \end{aligned} \quad (26)$$

As before, the smoothed \mathbf{b}_k should be normalized to eliminate the arbitrary value of the amplitude of \mathbf{b}_k and ascertain that the sum of \mathbf{b}_k is zero to satisfy the convergence condition of AO.

2.3. Image Acquisition

For evaluation of the above algorithms on actual brain images, dual fast spin echo (FSE) MR images of the whole brain (from vertex to foramen magnum) were acquired on 13 healthy normal volunteers (3 women and 10 men; age range 23 to 55 years). Since the dual echo images

are acquired in an interleaved manner, the images are in perfect registration with each other and do not require post-acquisition image alignment. Images were acquired either on a General Electric (1.5 T) or a Philips (3 T) scanner, with the following parameters: field-of-view of 240 mm \times 240 mm, image matrix of 256 \times 256, and echo train length of 8. A quadrature birdcage resonator was used both for RF transmission and signal reception at 1.5 T using the following parameters: TE1/TE2/TR = 12 ms/ 86 ms/6800 ms, where TE and TR represent the echo and repetition times respectively. A total of 42 contiguous and interleaved slices, each of 3 mm thick, were acquired. On the Philips 3T Intera scanner a six channel SENSE coil was used for signal reception while the whole body coil was used for RF transmission. A SENSE factor of 2 was used for these scans. MR images were acquired with the following scan parameters: TE1/TE2/TR = 9.5ms/90ms/6800 ms. The total number of slices at 3T was 44, each of 3 mm thick.

Prior to segmentation, the extrameningeal tissues from the images were removed using a semi-automatic procedure that is described elsewhere [12,29] and these stripped brain images were used as the input to the algorithms. The output of the algorithms included inhomogeneity corrected images, cluster centers, bias field, and memberships of the image volume. All the proposed algorithms were implemented under Interactive Data Language (IDL) environment in Windows.

2.4. Evaluation

Initially, the performance of the GFCM algorithm was evaluated quantitatively using the BrainWeb images. The BrainWeb images consist of 3 mm thick normal proton density (PD) and T2 weighted images with 3% noise and 40% inhomogeneity added. We assumed the number of clusters to be four and our results suggest this number to be appropriate (see the “Results and Discussion” for the rationale for using four clusters). For the BrainWeb images these four clusters represent white matter (WM), gray matter (GM), and cerebrospinal fluid (CSF), and dura matter that is consistent with Sucking et al. [30]. This is different from most of the studies performed using the single-channel images (such as T1 weighted) where usually only 3 classes - WM, GM, and CSF- are included [1, 20, 23, 34].

The convergence of clustering iterations is controlled by the L_2 norm of the cluster center’s difference between two consecutive iterations (denoted by ϵ). Two values for ϵ were used: $\epsilon=0.05$ and 0.01. At least visually, the clustering results for the two ϵ values were comparable, as assessed by an expert, but the computation cost for the smaller value of ϵ was almost twice. For instance, the computational time for AFCM was around 1 minute for $\epsilon=0.05$, but around 2 minutes for $\epsilon=0.01$. Therefore the value of $\epsilon=0.05$ was chosen to generate the initial inputs to the G-K algorithm using the AFCM. Other parameters that control the contextual constraints are indicated at the relevant places. All the segmentation (clustering) was performed in two-dimensional feature space.

For quantitative comparison of segmentation based on AFCM and G-K algorithms, we compared the tissue volumes (*Seg*) based on the segmentation of the BrainWeb images, with the reference volumes (*Ref*) generated by the ground truth (using the crisp data) and computing the four similarity measures defined in Eq. (27) – Eq. (30) [2]. In these equations, *POE*, *PUE*, *PCE* refer to the over-, under-, and the correctly estimated percentage of tissue volumes, respectively, and *SI* is the similarity index.

$$SI = \frac{2 \times (\text{Ref} \cap \text{Seg})}{\text{Ref} + \text{Seg}} \times 100 \quad (27)$$

$$POE = \frac{\overline{\text{Ref} \cap \text{Seg}}}{\text{Ref}} \times 100 \quad (28)$$

$$PUE = \frac{\text{Ref} \cap \overline{\text{Seg}}}{\text{Ref}} \times 100 \quad (29)$$

$$PCE = \frac{\text{Ref} \cap \text{Seg}}{\text{Ref}} \times 100 \quad (30)$$

The performance of the algorithm was also evaluated using the above procedure on the FSE images of normal human brain. In this case, the segmentation by an expert neurologist (more than 20 years of experience in MRI of MS) was considered as the ground truth. The segmentation by the expert was based on automatic segmentation using the method proposed by Sajja et al [29], followed by manual validation. For the FSE images these four classes primarily represent WM, GM, CSF, and GM+CSF. Without the inclusion of GM+CSF as a separate cluster, the large spread between GM and CSF in the feature space led to less favorable classification results.

3. Results and Discussion

The BrainWeb images were segmented into four tissue classes: WM, GM, CSF, and dura matter. The intensity inhomogeneity correction was performed iteratively along with the classification of tissues as described in the "Methods and Materials". As mentioned earlier, the BrainWeb images were classified using the neighborhood contextual constraint based on intensity [1]. In these studies α was set to 0.01 to balance between the ability in overcoming noise and the effect of blurring the segmentation; the power of the membership, p , was set to 2 for all studies. For the contextual constraints in 3D the direct neighborhood was set to 26. We observed that the inclusion of neighborhood contextual constraints in the AO iterations did slow down the process significantly. Therefore, the contextual constraints were applied only when the clustering without contextual constraints was completed. The iteration with contextual constraints required only limited number of loops (one loop in our studies).

As an example, images segmented using the GFCM along with the corresponding BrainWeb image at one slice location are shown in Figure 1. As can be seen from these images, GFCM, at least visually, has provided quite satisfactory results. Table 1 summarizes the quantitative evaluation of AFCM and GFCM based on the similarity measures for all the segmented tissues. The performance of GFCM can be appreciated by the high values of the similarity index. A comparison of the results in Tables 1 clearly shows that G-K algorithm improved all the similarity measures.

The FSE images were classified into four classes: GM, WM, CSF and GM+CSF. The use of four clusters in the FSE images (GM, WM, CSF, GM+CSF) can also be rationalized by the fact that the proximity of CSF and GM, particularly in the cortex, often results in significant overlap between these two tissues. As an example Figure 2 shows the segmentation (membership) of one section of brain in the cerebellar region. It is known that on the FSE images the tissue intensities in the cerebellar regions are different from those of the superior parts of the brain [30]. These intensity differences can not be corrected by merely applying the inhomogeneity correction. Therefore, the cerebellar and the posterior fossa regions are very difficult to segment using automatic techniques [29,30,34] and the segmentation of the cerebellum area is usually performed by adopting regional or localized methods [29,30,34]. Thus, it is gratifying that segmentation of the cerebellar region has been considerably improved with GFCM.

Inclusion of the G-K algorithm to account for the nonspherical occupancy of the feature space is a major component of GFCM. Therefore, we quantitatively evaluated the importance of G-K algorithm by segmenting the Brain Web and FSE images with and without incorporation of

the G-K algorithm and comparing the results with the ground truth using the similarity measures described above. The improvement in the tissue segmentation by including the G-K algorithm was also visually evaluated on the FSE images. Figure 3 shows the segmentation of Brain Web images with and without the contextual constraints for G-K algorithm, and Table 1 summarizes the quantitative comparisons. After the G-K algorithm without the contextual constraints was completed, only a single iteration was performed following the application of the contextual constraints. It is important to point out that the inclusion of neighborhood intensity based contextual constraint places increased computational burden. Further optimization of α and number of iterations is necessary for improving the performance of contextual constraint.

The same iteration stop criteria and contextual constraints used for the Brain Web images were employed for the FSE images. It should be pointed out that the FSE images were hard segmented to include only the three pure classes, GM, WM, and CSF (through winner takes all on the membership). Inclusion of three pure classes is necessary since the mixed class can not be delineated by the human expert. Table 2 – Table 5 summarize the SI, POE, PUE and PCE for the FSE images on 13 normal volunteers. Figure 4 shows the similarity measures (SI and PCE) for all the 13 FSE images with contextual constraints for $\alpha=0.01, 0.001, 0.005,$ and 0.0005 . It can be seen from these plots that the results are relatively insensitive to the value of α over a wide range. Because of the space limitations, we included only SI and PCE, the two more important similarity measures, in these plots.

Figure 5 shows the PD and T2 weighted FSE images at different locations. The corresponding segmented images with AFCM, GFCM, and GFCM with contextual constraint ($\alpha=0.01$) are shown in Figs. 5c–e, respectively. Consistent with the quantitative analysis based on the similarity measures, these images demonstrate that visually GFCM performed better than AFCM, and GFCM with and without contextual constraint provided comparable results.

It is difficult to quantitatively compare our results with other published results since very few publications evaluated the performance of the segmentation using the metrics employed in the current studies. Of the four similarity measures employed in these studies, SI is considered to be the most important metric since it is a measure of the agreement between the proposed segmentation and the ground truth. Higher the SI value, better is the agreement. The high SI values (~90%) that we achieved for segmented BrinWeb images, where the ground truth is known, suggests excellent performance of the GFCM method. The SI value for the FSE images, however, is slightly lower, particularly for the CSF. This slightly lower value perhaps is due to the fact that the ground truth is not known in this case. Our results also demonstrate the improved performance of GFCM relative to AFCM. We did not observe significant differences in the segmentation quality by including the contextual constraint. However, this conclusion is based on limited studies without complete optimization of the parameters (α and number of iterations).

In these studies we have included only normal brains. Additional dimensions (such as FLAIR images) in the feature space may be required to increase the separability of more classes such as lesions [3,13,16].

5. Conclusions

A comprehensive GFCM technique for multispectral segmentation of MR images is described. This technique incorporates an efficient bias field correction along with contextual constraints. In addition, this method takes into account the nonspherical occupancy of the feature space by replacing the Euclidean distance with cluster scatter measures to define the Mahalanobis

distance. Qualitative and quantitative evaluation on Brain Web and real brain images indicates that GFCM outperforms the AFCM method.

Acknowledgments

This work is supported by the National Institutes of Health grants EB002095 and 1 S10 RR19186. We acknowledge Vipulkumar Patel for acquiring the FSE images.

References

1. Ahmed MN, Yamany SM, Mohamed N, Farag AA, Moriarty T. A modified fuzzy c-means algorithm for bias field estimation and segmentation of MRI data. *IEEE Trans Med Imag* 2002;21:193–199.
2. Anbeek P, Vincken KL, van Osch MJP, Bisschops RHC, Grond J. Probabilistic segmentation of white matter lesions in MR imaging. *NeuroImage* 2004;21:1037–1044. [PubMed: 15006671]
3. Bedell BJ, Narayana PA, Wolinsky JS. A dual approach for minimizing false lesion classifications on magnetic resonance images. *Magn Reson Med* 1997;37:94–102. [PubMed: 8978637]
4. Bermel RA, Bakshi R. The measurement and clinical relevance of brain atrophy in multiple sclerosis. *Lancet Neurol* 2006;5:158–170. [PubMed: 16426992]
5. Bensaid AM, Hall LO, Bezdek JC, Clarke LP. Partially supervised clustering for image segmentation. *Pattern Recognition* 1996a;29:859–871.
6. Bensaid AM, Hall LO, Bezdek JC, Clarke LP, Silbiger ML, Arrington JA, Murtagh RF. Validity-guided reclustering with applications to image segmentation. *IEEE Trans Fuzzy Syst* 1996b;4:112–123.
7. Bezdek, JC. PhD thesis. Cornell University; 1973. Fuzzy Mathematics in Pattern Classification.
8. Bezdek JC, Ehrlich R, Full W. FCM: Fuzzy c-Means Algorithm. *Computers and Geoscience* 1984;10:191–203.
9. Borgelt, C.; Kruse, R. Shape and size regularization in expectation maximization and fuzzy clustering; *Proc 8th Euro Conf Principles Practice Knowledge Discovery Databases (PKDD)*; 2004. p. 52-62.
10. Clark MC, Hall LO, Goldgof DB, Clarke LO, Velthuizen RP, Silbiger MS. MRI segmentation using fuzzy clustering techniques. *IEEE Eng Med Bio* 1994;13:730–742.
11. Cocosco CA, Kollokian V, Kwan RK-S, Evans AC. Brain Web: online interface to a 3D MRI simulated brain database. *NeuroImage* 1997;5:S425–S427.
12. Datta S, Sajja BR, He R, Wolinsky JS, Gupta RK, Narayana PA. Segmentation and quantification of black holes in multiple sclerosis. *Neuroimage* 2006;29:467–474. [PubMed: 16126416]
13. Ding Z, Preiningerova J, Cannistraci CJ, Vollmer TL, Gore JC, Anderson AW. Quantification of multiple sclerosis lesion load and brain tissue volumetry using multiparameter MRI: methodology and reproducibility. *Magn Reson Imag* 2005;23:445–452.
14. Gunn JC. A fuzzy relative of the ISODATA process and its use in detecting compact, well separated clusters. *J Cybern* 1974;3:95–104.
15. Gustafson, DE.; Kessel, WC. Fuzzy clustering with a fuzzy covariance matrix; *Proc IEEE Conf Decision Contr*; 1979. p. 1761-1766.
16. He R, Sajja BR, Narayana PA. Implementation of high dimensional feature map for segmentation of MR images. *Annals Biomed Engg* 2005;33:1439–1448.
17. Höppner, F.; Klawonn, F.; Kruse, R.; Runkler, TA. *Fuzzy Cluster Analysis*. 1st ed.. Chichester: Wiley; 1999.
18. [http://www.bic.mni.mcgill.ca/Brain Web/](http://www.bic.mni.mcgill.ca/Brain%20Web/)
19. Inglese M, Grossman RI, Filippi M. Magnetic resonance imaging monitoring of multiple sclerosis lesion evolution. *J Neuroimaging* 2005;15:22S–29S. [PubMed: 16385016]
20. Jiang, L.; Yang, W. A modified fuzzy c-means algorithm for segmentation of magnetic resonance images. *Proceedings of the Seventh International Conference on Digital Image Computing: Techniques and Applications*; Sydney. CSIRO Publishing; 2003. p. 225-232.
21. Keller, A.; Klawonn, F. Adaptation of cluster sizes in objective function based fuzzy clustering. In: Leondes, CT., editor. *Database and Learning Systems IV*. Boca Raton: CRC Press; 2003. p. 181-199.

22. Li DK, Li MJ, Traboulsee A, Zhao G, Riddehough A, Paty D. The use of MRI as an outcome measure in clinical trials. *Adv Neurol* 2006;98:203–226. [PubMed: 16400836]
23. Liew AW-C, Yan H. An adaptive spatial fuzzy clustering algorithm for 3-D MR image segmentation. *IEEE Trans Med Imag* 2003;22:1063–1075.
24. Liew AW-C, Yan H. Current methods in automatic tissue segmentation of 3D magnetic resonance brain images. *Curr Med Imaging Rev* 2006;2:91–103.
25. Lycklama a Nijeholt GJ. Reduction of brain volume in MS. MRI and pathology findings. *J Neurol Sci* 2005;233:199–202. [PubMed: 15949505]
26. Matthews B, Siemers ER, Mozley PD. Imaging-based measures of disease progression in clinical trials of disease-modifying drugs for Alzheimer disease. *Am J Geriatr Psychiatry* 2003;11:146–159. [PubMed: 12611744]
27. Pham DL. Spatial models for fuzzy clustering. *Computer Vision and Image Understanding* 2001;84:285–297.
28. Pham DL, Prince JL. Adaptive fuzzy segmentation of magnetic resonance images. *IEEE Trans Med Imag* 1999;18:737–752.
29. Sajja BR, Datta S, He R, Mehta M, Gupta RK, Wolinsky JS, Narayana PA. Unified approach for multiple sclerosis lesion segmentation on brain MRI. *Annals Biomed Engg* 2006;34:142–151.
30. Suckling J, Sigmundsson T, Greenwood K, Bullmore ET. A modified fuzzy clustering algorithm for operator independent brain tissue classification of dual echo MR images. *Magn Reson Imag* 1999;17:1065–1076.
31. Sutton, MA.; Bezdek, JC.; Cahoon, TC. Image segmentation by fuzzy clustering: methods and issues. In: Bankman, IN., editor. *Handbook of Medical Imaging: Processing and Analysis*. San Diego: Academic Press; 2000. p. 87-106.
32. Taxt T, Lundervold A. Multispectral analysis of the brain using magnetic resonance imaging. *IEEE Trans Med Imag* 1994;13:470–481.
33. Xue J-H, Pizurica A, Philips W, Kerre E, van De Walle R, Lemachieu I. An integrated method of adaptive enhancement for unsupervised segmentation of MRI brain images. *Pattern Recognition Letters* 2003;24:2549–2560.
34. Zhu C, Jiang T. Multicontext fuzzy clustering for separation of brain tissues in magnetic resonance images. *NeuroImage* 2003;18:685–696. [PubMed: 12667846]

Biographies

Renjie He, He got his Ph.D. in Electrical Engineering with specialization in Biomedical Engineering from Tsinghua University, Beijing, China, in 1998, he is assistant professor with Department of Diagnostic and Interventional Imaging, University of Texas Medical School at Houston.

Sushmita Datta, She got her Ph.D. in mathematics form Indian Institute of Technology, Kanpur, India, in 2003, she is research associate of Department of Diagnostic and Interventional Imaging, University of Texas Medical School at Houston.

Balasrinivasa Rao Sajja, He got his Ph.D. in mathematics form Indian Institute of Technology, Kanpur, India, in 2002, he is assistant professor with Department of radiology, University of Nebraska Medical Center.

Ponnada Narayana, He got his Ph.D. in Physics from Indian Institute of Technology, Kanpur, India, in 1969, He is professor with Department of Diagnostic and Interventional Imaging, University of Texas Medical School at Houston.

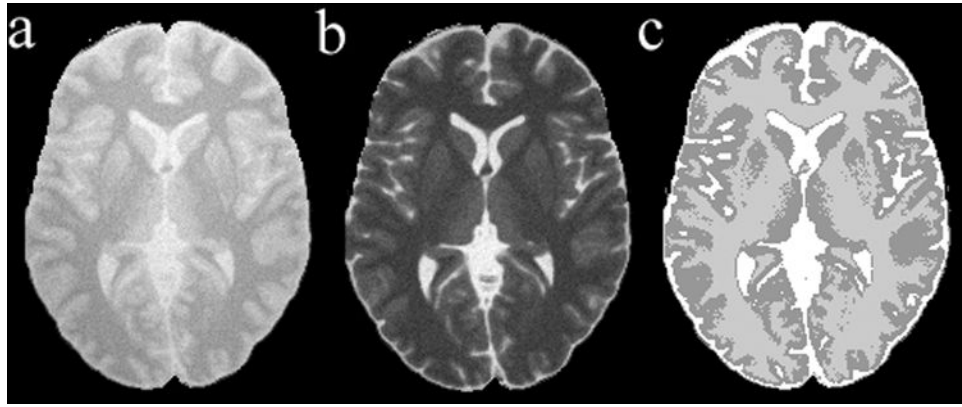


Figure 1. (a) and (b) Axial cross-section of Brain Web (PD and T2) images, (c) Classification of WM (gray), GM (dark), CSF (bright) based on GFCM.

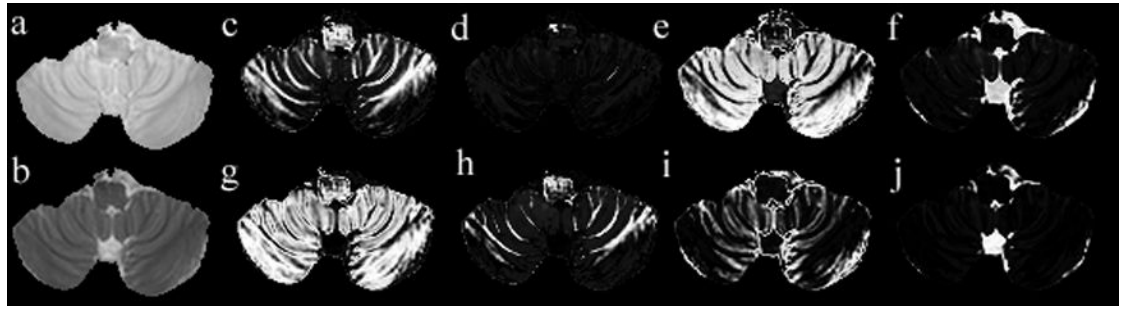


Figure 2. Axial FSE images in the cerebellum region. (a) and (b), AFCM membership (c) to (f) and GFCM membership (g) to (j) Classification is based on WM, GM, GM+CSF, and CSF, respectively.

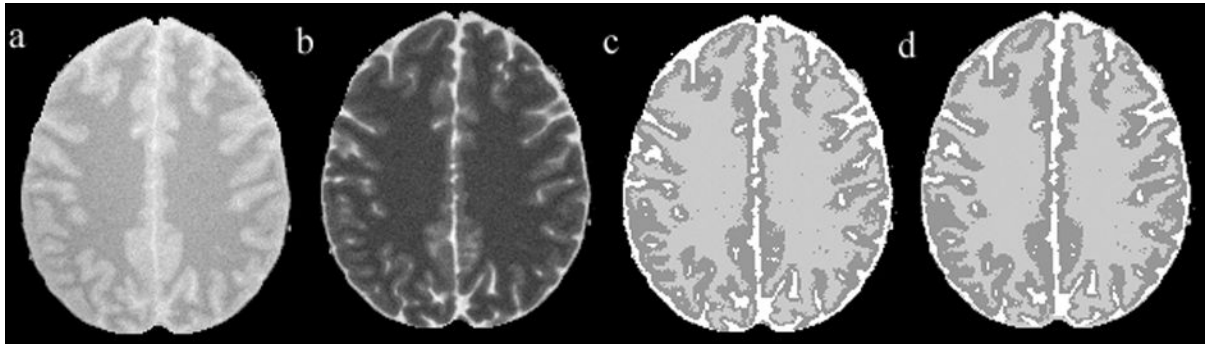
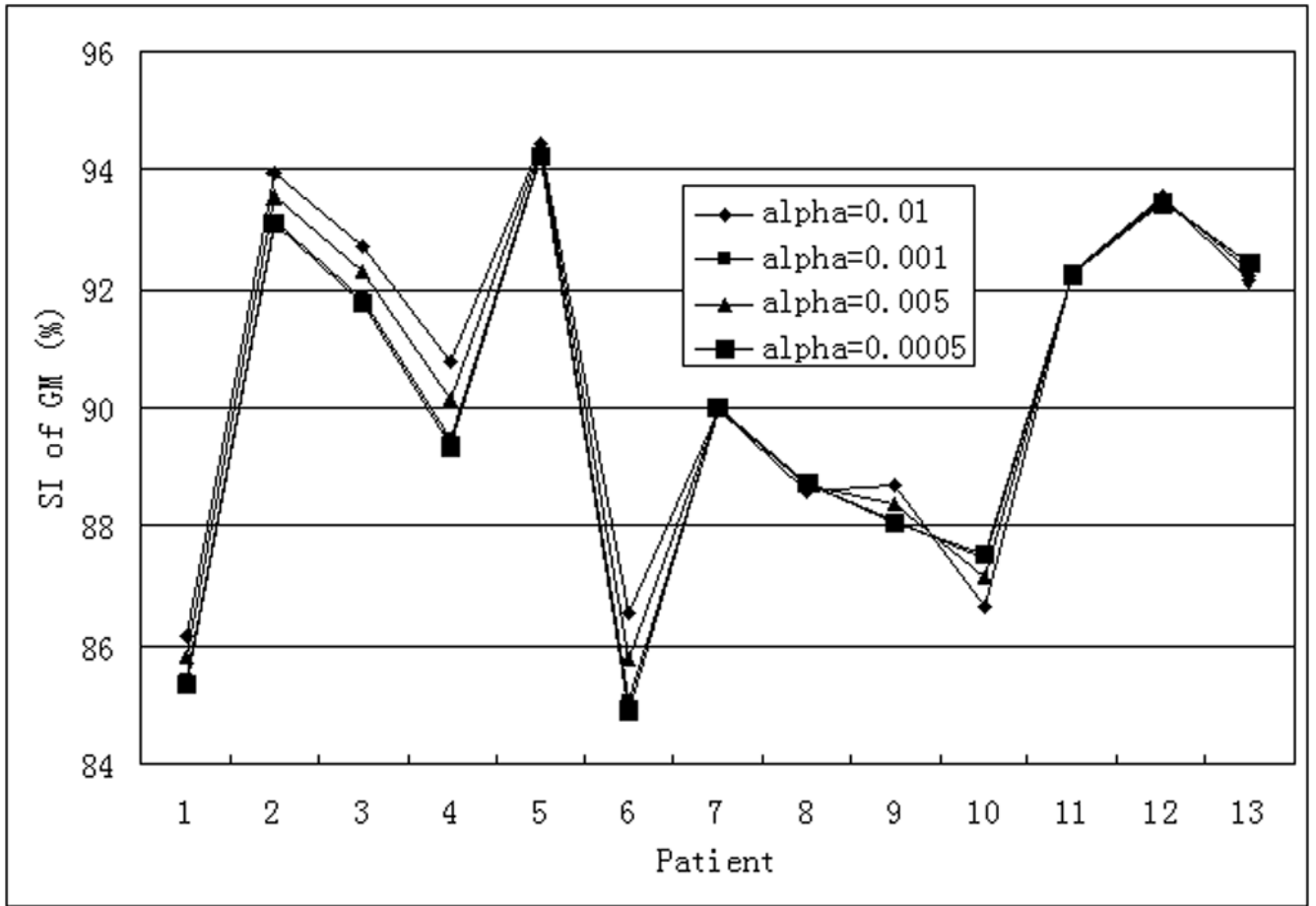
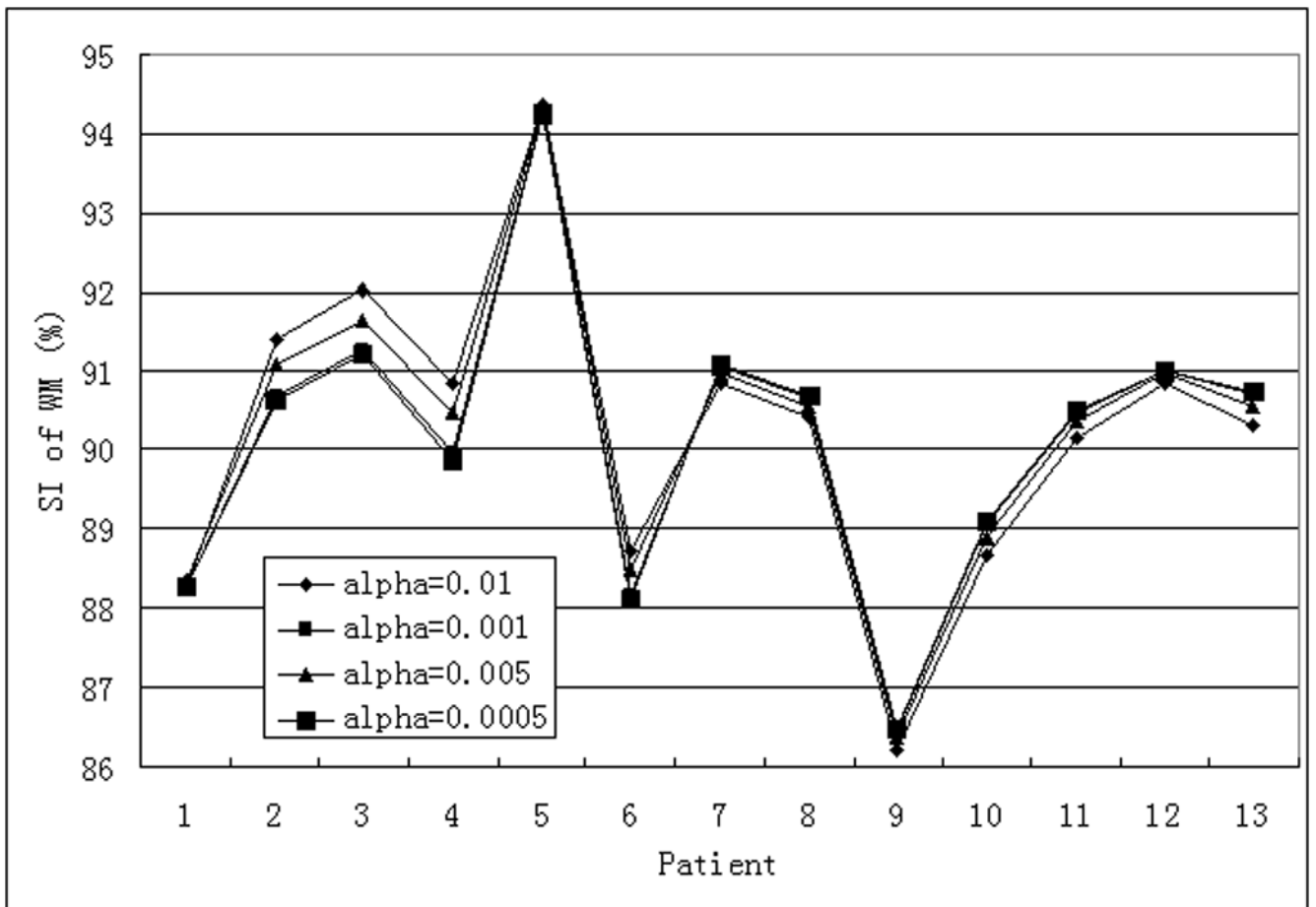
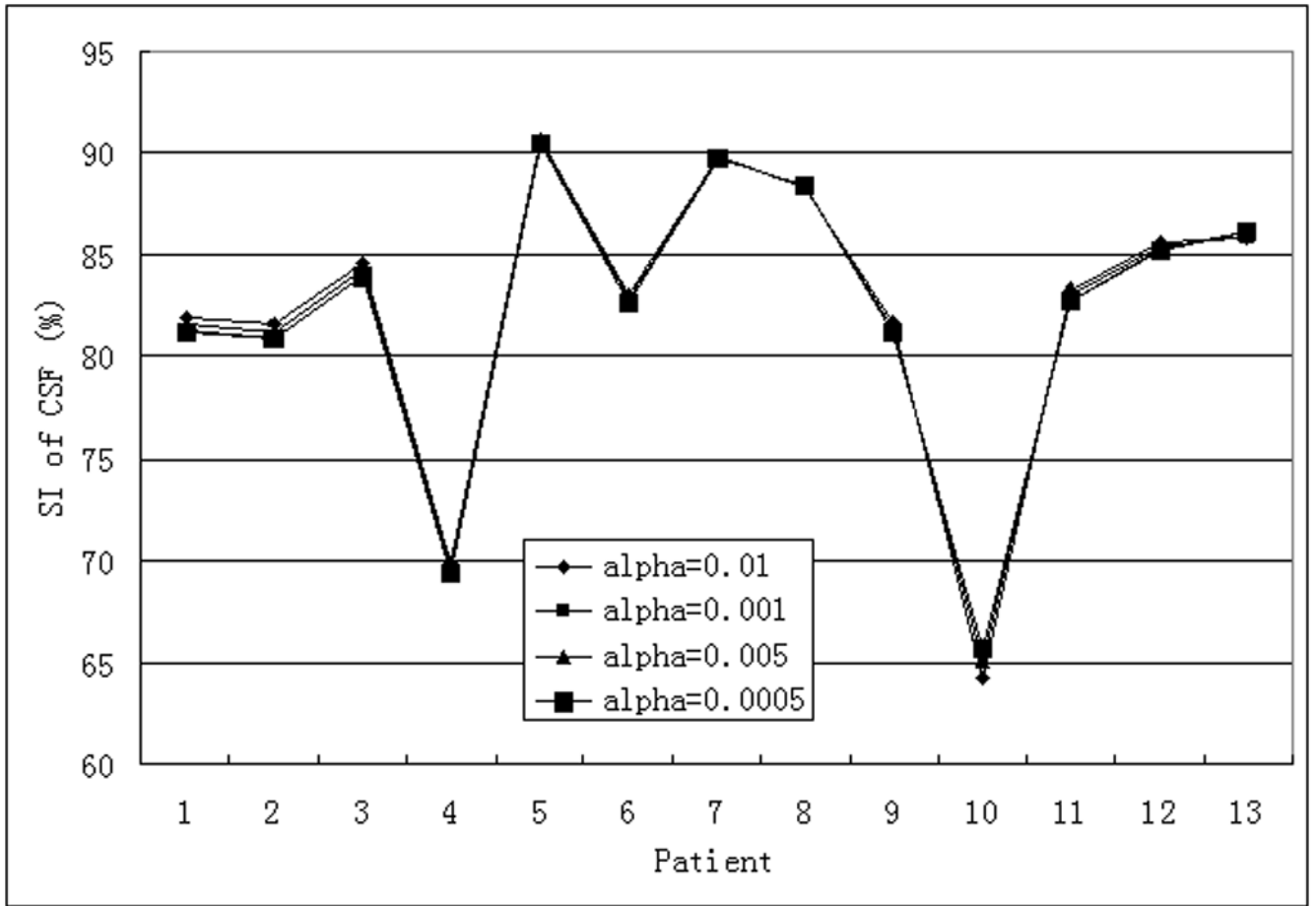


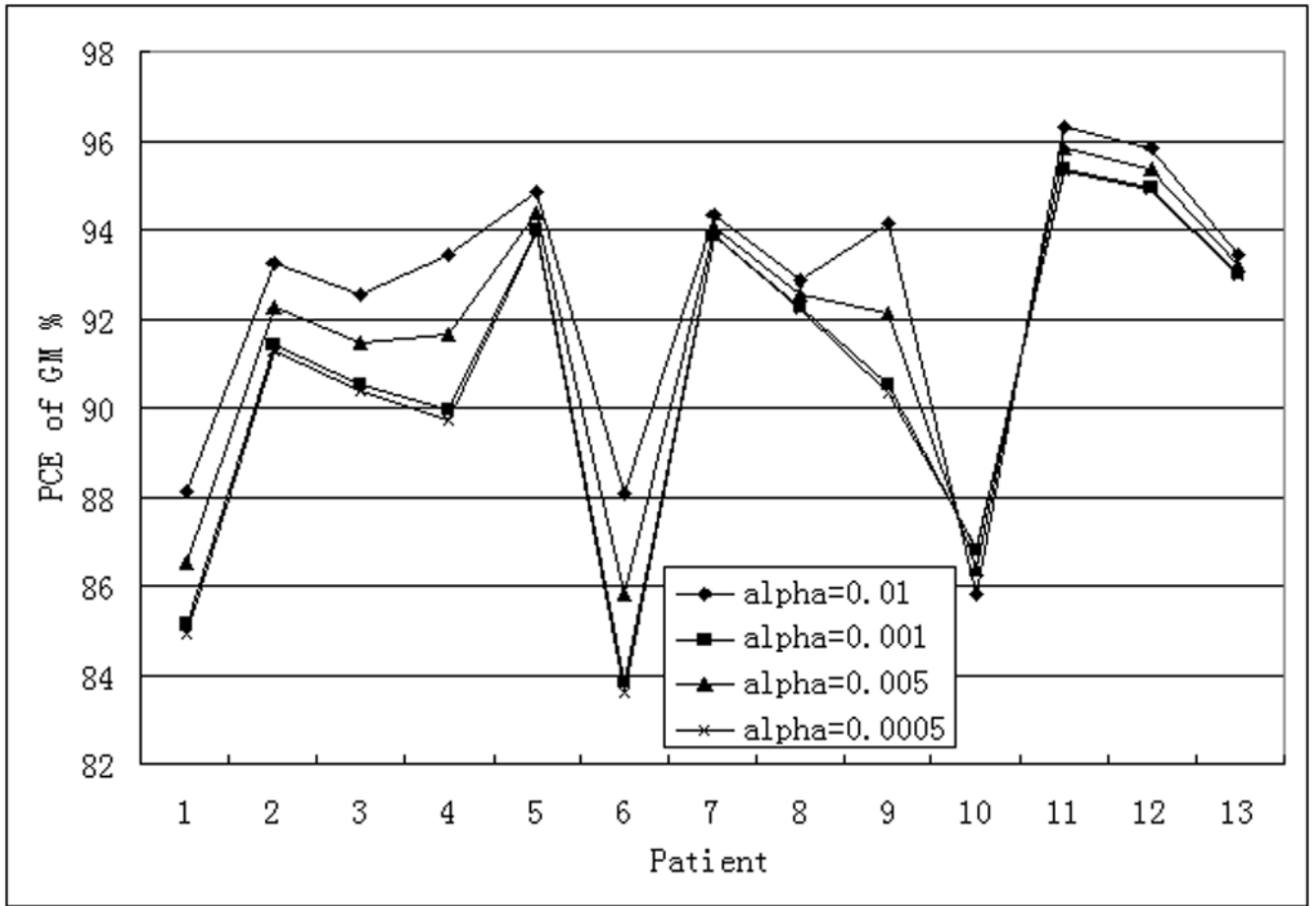
Figure 3.

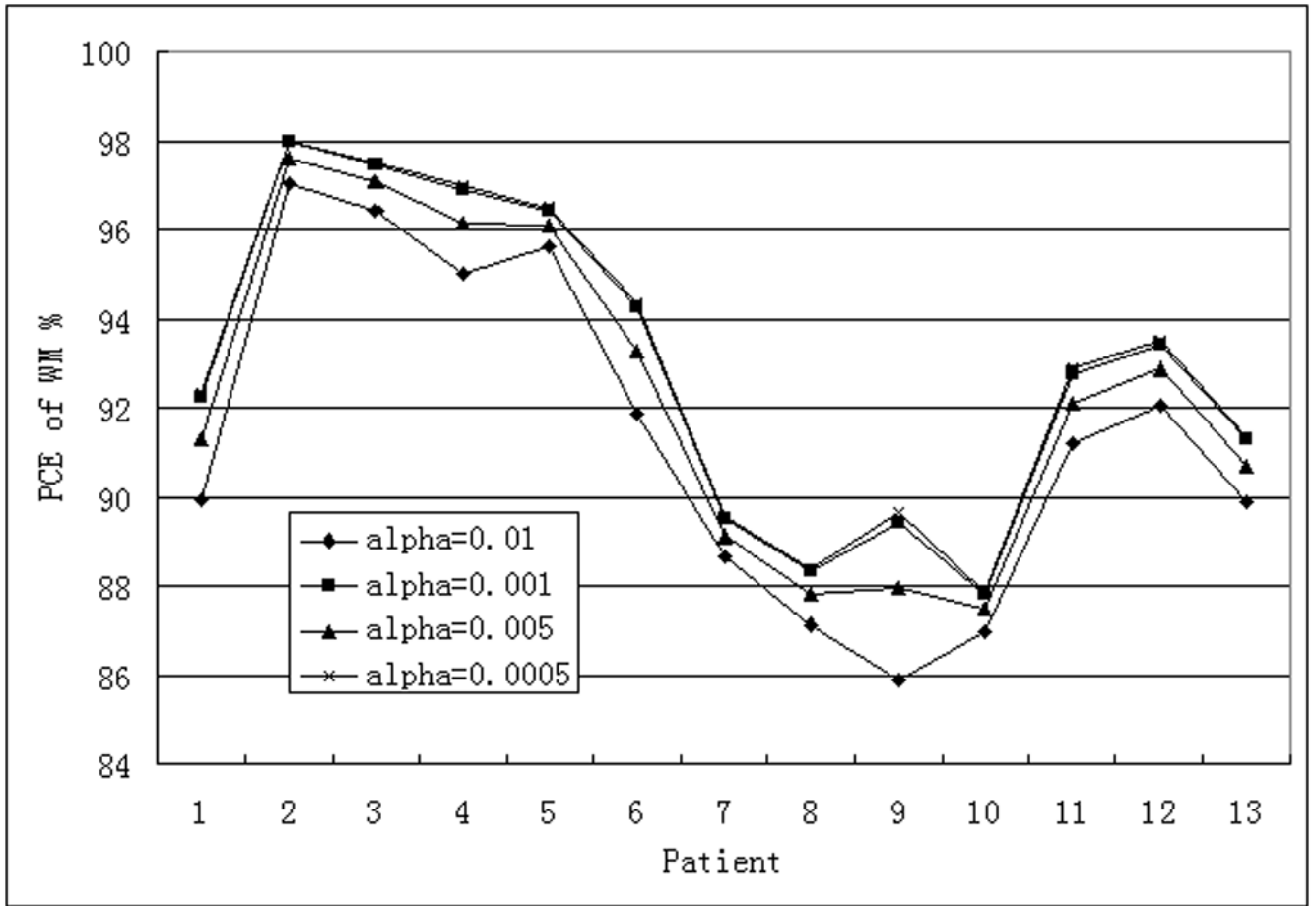
Effect of the inclusion of contextual constraints on the GFCM classification. The PD and T2 Brain Web images are shown in (a) and (b), respectively. Images (c) and (d) demonstrate classification before and after the application of the neighborhood intensity based contextual constraint, respectively.











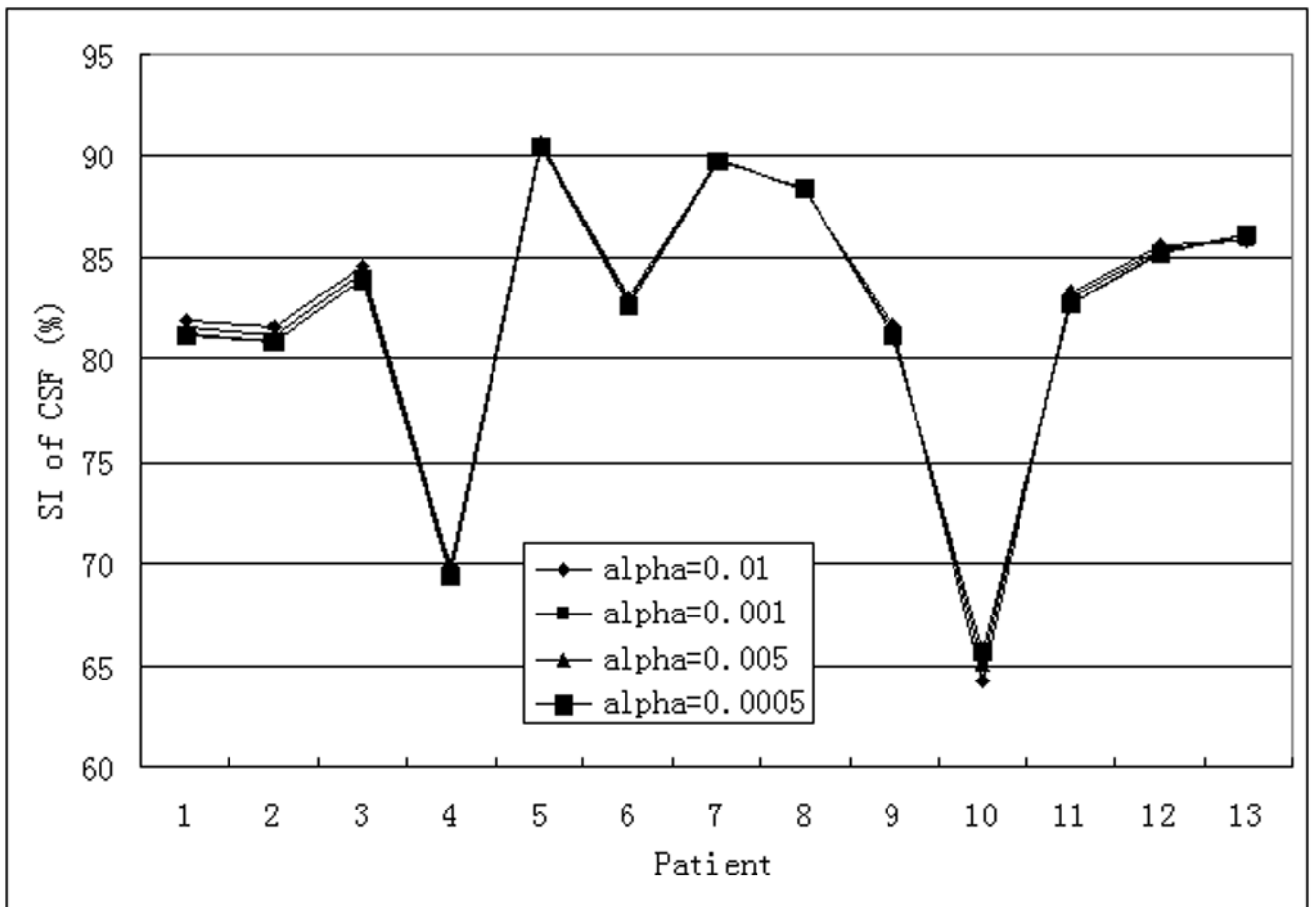
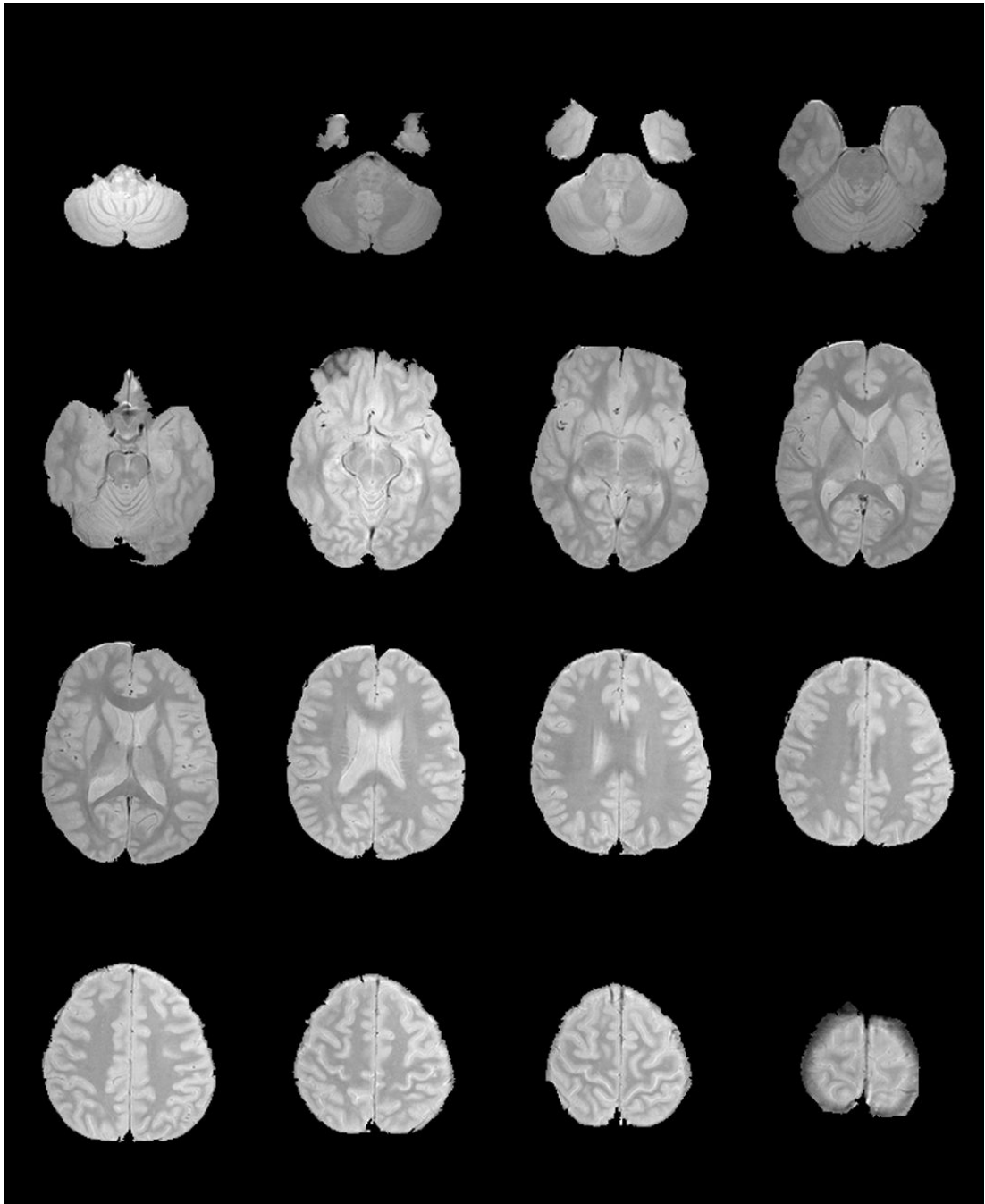
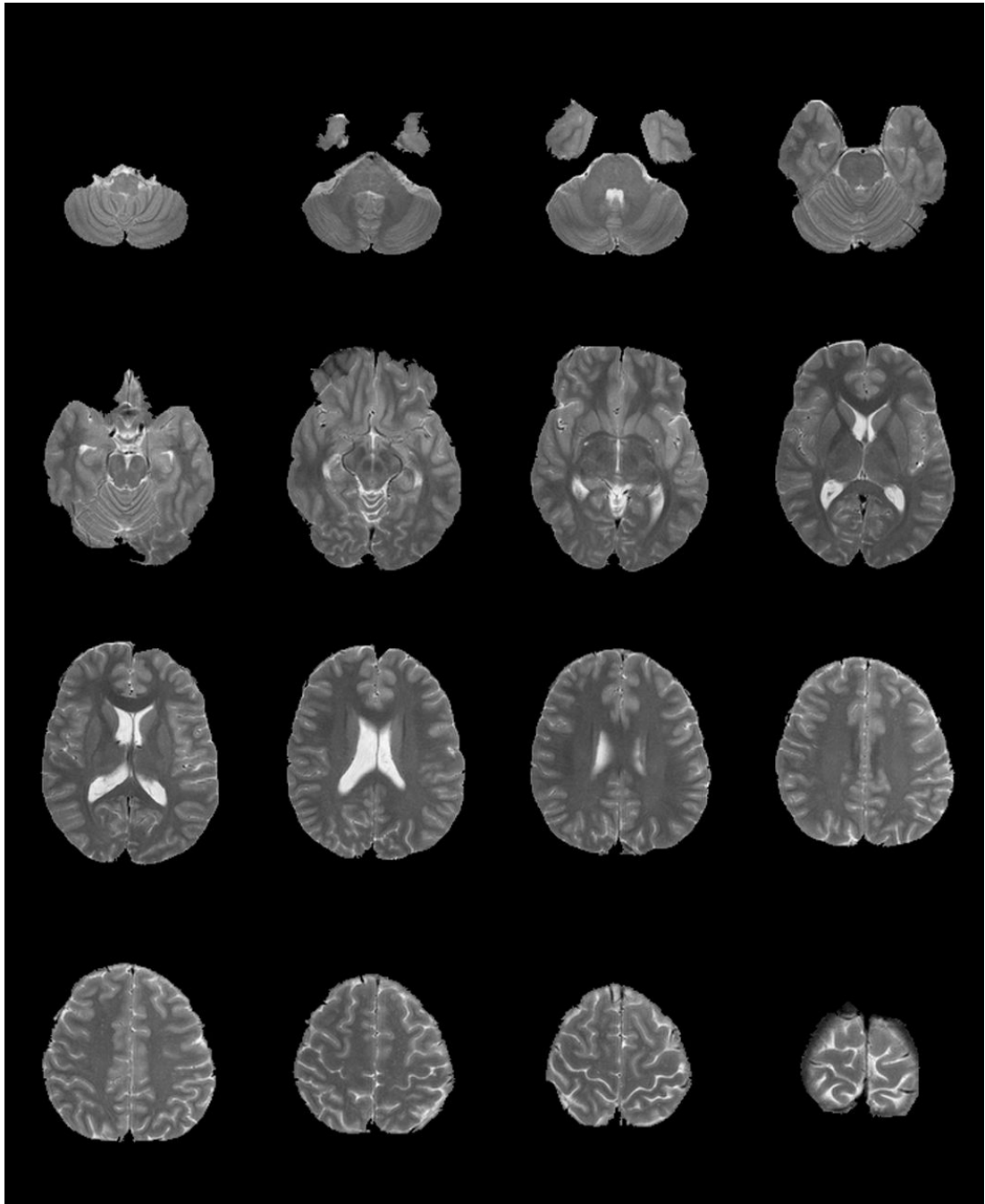
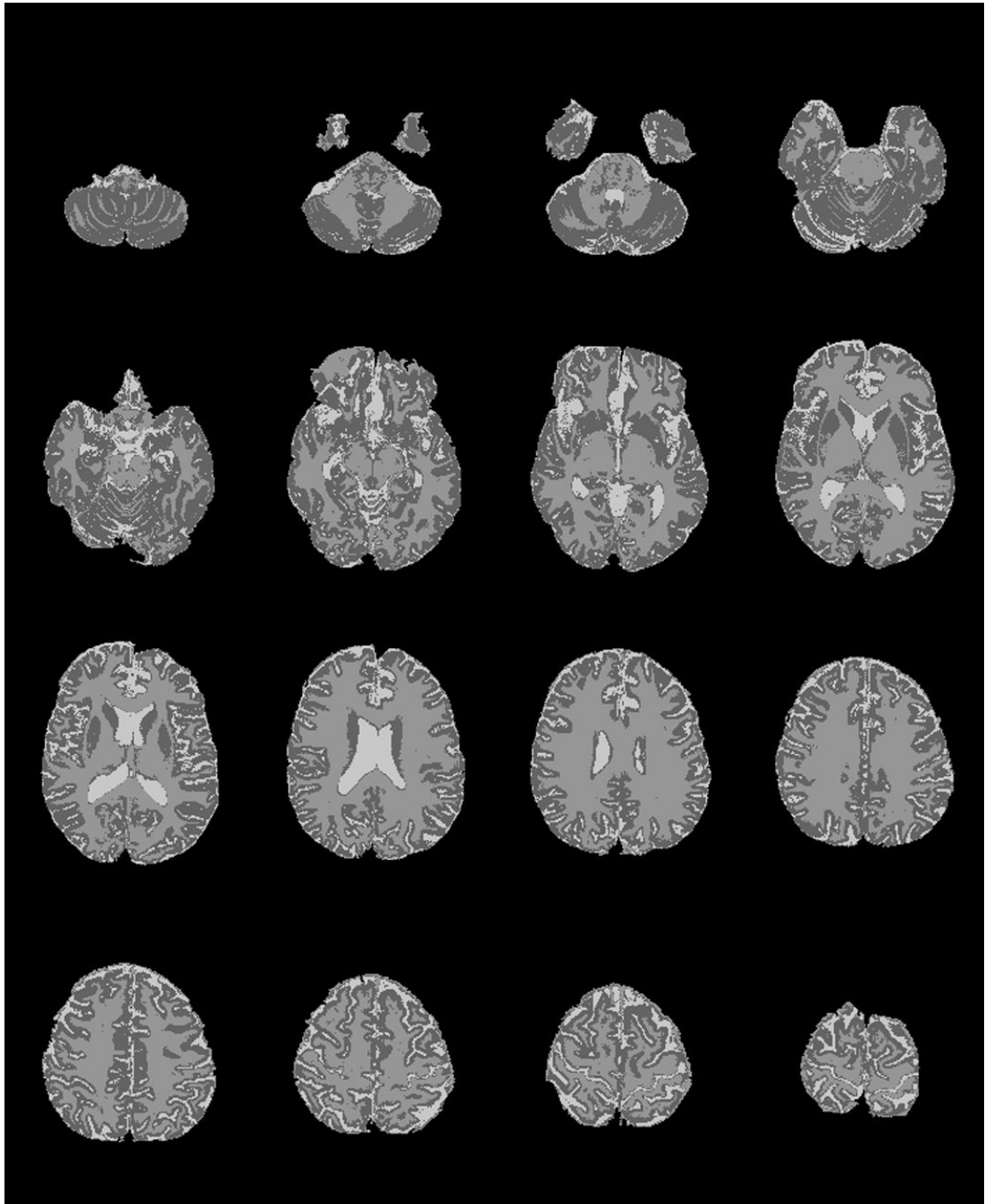
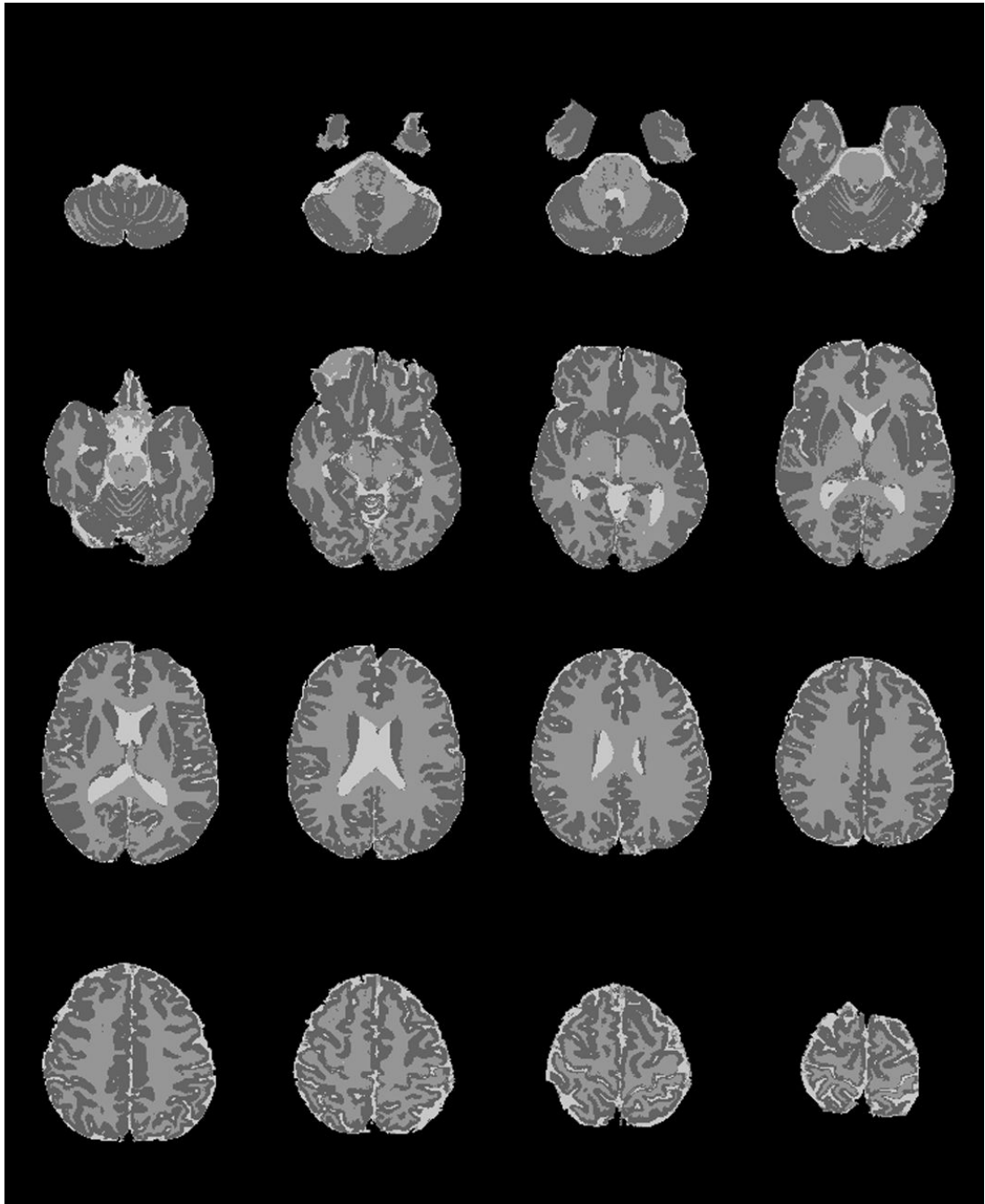


Figure 4. Values of SI ((a) to (c)) and PCE ((d) to (f)) for GM ((a) and (d)), WM ((b) and (e)) and CSF ((c) and (f)) for the 13 FSE images with $\alpha=0.01$, $\alpha=0.001$, $\alpha=0.005$, and $\alpha=0.0005$.









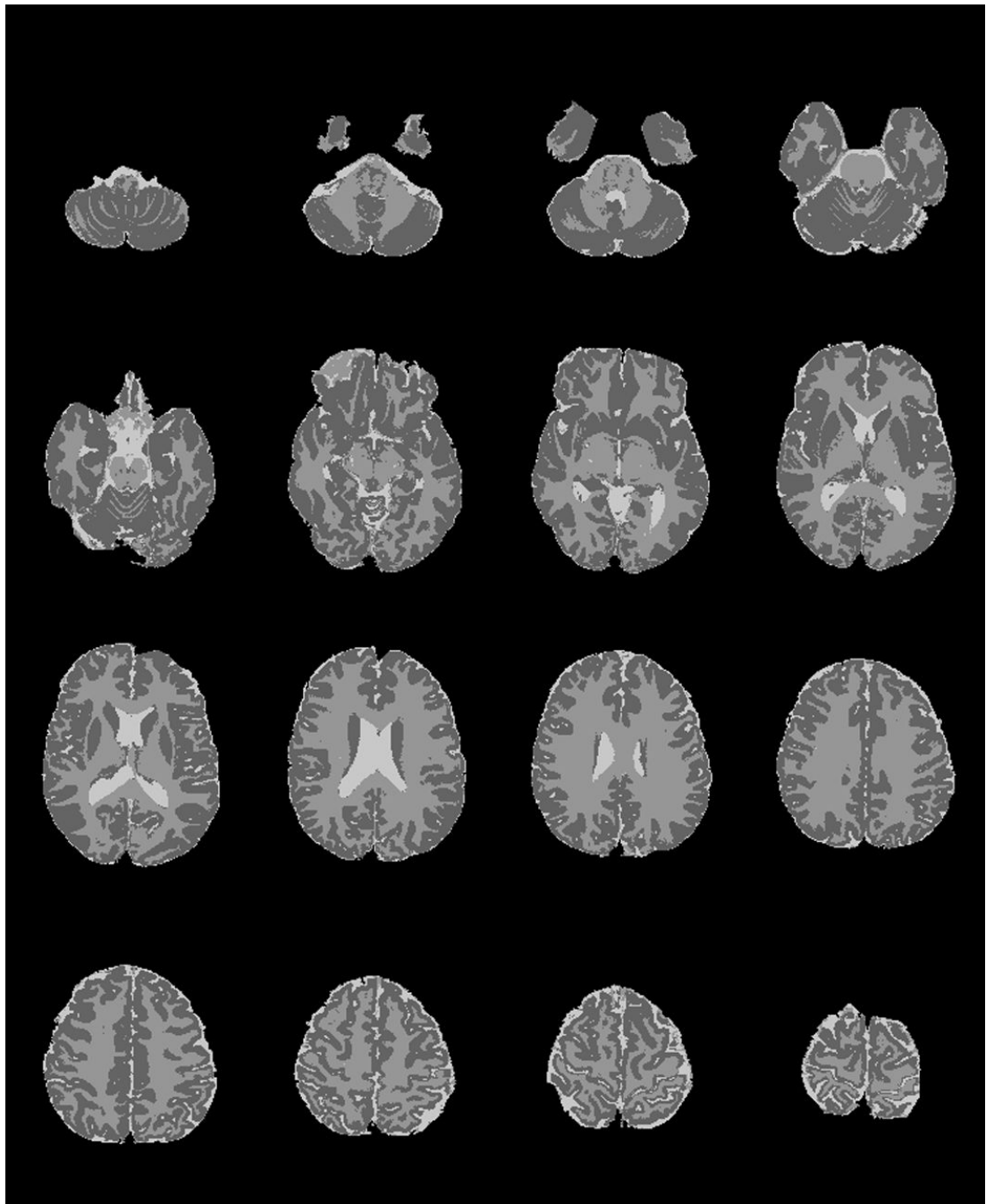


Figure 5. Typical FSE volume images (PD (a) and T2 (b) and segmented images using AFM (c), GFCM (d), and GFCM with contextual constraint ($\alpha=0.01$) (e). In the segmented images, dark, grey, and bright represent GM, WM, and CSF, respectively.

Table 1

Similarity measures based on AFCM and GFCM without and with neighborhood contextual constraints ($\alpha=0.01$, one loop in iterations) on the Brain Web images. The similarity measures are expressed as %.

	AFCM			GFCM			GFCM+ α		
	GM	WM	CSF	GM	WM	CSF	GM	WM	CSF
SI	89.7275	75.5651	73.3794	89.6643	88.7303	97.7046	91.2838	90.6280	98.8351
POE	6.5546	10.0034	72.1330	5.83764	14.9534	4.4711	3.4493	14.9132	1.9871
PUE	13.2976	33.1987	0.2452	13.9910	8.3321	0.2174	13.1386	4.7804	0.3616
PCE	86.7024	66.8013	99.7548	86.0090	91.6679	99.7826	86.8614	95.2196	99.6384

Table 2
 Similarity Index (SI, expressed as %) calculated on 13 FSE images. The SI values were calculated for both AFCM and GFCM without neighborhood contextual constraints.

SI	AFCM			GFCM		
	GM	WM	CSF	GM	WM	CSF
	79.4727	89.1956	65.1268	84.6939	92.3825	71.8066
	77.4859	94.5355	57.9352	91.1714	98.0235	70.0469
	78.1612	93.7035	67.5857	90.2955	97.499	75.4679
	78.5093	88.3633	60.8767	89.4157	97.039	55.5004
	82.1223	90.9386	73.9443	93.8807	96.4918	86.1914
	81.3736	90.2402	71.0513	83.228	94.4126	72.9011
	76.7665	92.876	73.6889	93.6862	89.5908	86.0381
	82.2208	89.7945	74.5424	91.894	88.4854	87.7143
	82.5891	87.2643	60.275	90.1525	89.7425	70.0731
	77.3762	91.7311	64.0416	86.784	87.8354	74.108
	84.2675	95.4521	62.1292	95.2461	92.8786	71.6463
	86.1678	94.3212	62.0867	94.8094	93.5145	77.0576
	84.5455	94.444	69.1983	92.8593	91.3512	84.0477
Mean	80.85065	91.75845	66.34478	90.62436	93.01898	75.58457
STD	3.096724	2.666064	5.707285	3.787879	3.519487	8.88022

Table 3
 Percentage of overestimated (POE, expressed as %) tissue volumes calculated on 13 FSE images. The POE values were calculated for both AFCM and GFCM without neighborhood contextual constraints.

	AFCM			GFCM		
	GM	WM	CSF	GM	WM	CSF
POE	17.9762	17.8663	23.2893	14.0027	17.1144	4.71735
	8.67723	19.2238	63.6992	4.75687	18.4199	3.1987
	10.4612	19.3913	41.0715	6.56165	16.4028	4.33203
	15.2508	17.0538	49.1291	11.0201	19.1844	4.51201
	12.7689	9.37141	46.1973	5.36725	8.32075	4.37524
	16.4606	18.8362	14.6842	13.1269	20.1573	3.2194
	16.8589	19.4169	9.86459	14.6528	7.20396	5.82454
	19.5846	10.8091	22.771	15.5026	6.73756	11.1286
	20.3589	19.5538	18.9921	14.7261	17.8364	2.42607
	11.8643	11.0086	80.251	11.6301	9.3917	51.8229
	13.118	19.1279	13.5366	11.2753	12.4175	1.3909
	12.0159	15.6141	23.1833	8.13183	12.1234	3.76708
	10.0812	14.8677	24.3759	8.16691	10.0355	11.487
Mean	14.26744	16.31853	33.15731	10.68624	13.48812	8.630909
STD	3.7561	3.70281	21.38862	3.729274	4.875732	13.3231

Percentage of underestimated (PUE, expressed as %) tissue volumes calculated on 13 FSE images. The PUE values were calculated for both AFCM and GFCM without neighborhood contextual constraints.

Table 4

	AFCM			GFCM		
	GM	WM	CSF	GM	WM	CSF
PUE	20.5273	10.8044	34.8732	15.3061	7.6175	28.1934
	22.5141	5.46448	42.0648	8.82858	1.9765	29.9531
	21.8388	6.29653	32.4143	9.70451	2.50097	24.5321
	21.4907	11.6368	39.1233	10.5843	2.96104	44.4996
	17.8777	9.06141	26.0557	6.11927	3.50823	13.8086
	18.6264	9.75982	28.9487	16.772	5.58736	27.0989
	23.2335	7.12396	26.3111	6.31383	10.4092	13.9619
	17.7792	10.2055	25.4576	8.106	11.5146	12.2857
	17.4109	12.7357	39.725	9.8475	10.2575	29.9269
	22.6238	8.26889	35.9584	13.216	12.1646	25.892
	15.7325	4.54785	37.8708	4.75391	7.12143	28.3537
	13.8322	5.6788	37.9133	5.19056	6.48545	22.9424
	15.4545	5.55601	30.8017	7.1407	8.64882	15.9523
Mean	19.14935	8.24155	33.65522	9.375635	6.981015	24.41543
STD	3.096724	2.666082	5.707285	3.787883	3.519487	8.88022

Table 5 Percentage of correctly estimated (PCE, expressed as %) tissue volumes calculated on 13 FSE images. The PCE values were calculated for both AFCM and GFCM without neighborhood contextual constraints

	AFCM			GFCM		
	GM	WM	CSF	GM	WM	CSF
PCE	79.4727	89.1956	65.1268	84.6939	92.3825	71.8066
	77.4859	94.5355	57.9352	91.1714	98.0235	70.0469
	78.1612	93.7035	67.5857	90.2955	97.499	75.4679
	78.5093	88.3633	60.8767	89.4157	97.039	55.5004
	82.1223	90.9386	73.9443	93.8807	96.4918	86.1914
	81.3736	90.2402	71.0513	83.228	94.4126	72.9011
	76.7665	92.876	73.6889	93.6862	89.5908	86.0381
	82.2208	89.7945	74.5424	91.894	88.4854	87.7143
	82.5891	87.2643	60.275	90.1525	89.7425	70.0731
	77.3762	91.7311	64.0416	86.784	87.8354	74.108
	84.2675	95.4521	62.1292	95.2461	92.8786	71.6463
	86.1678	94.3212	62.0867	94.8094	93.5145	77.0576
	84.5455	94.444	69.1983	92.8593	91.3512	84.0477
Mean	80.85065	91.75845	66.34478	90.62436	93.01898	75.58457
STD	3.096724	2.666064	5.707285	3.787879	3.519487	8.88022